nature nanotechnology

SUPPLEMENTARY INFORMATION

DOI: 10.1038/NNANO.2014.187

Twist-controlled resonant tunnelling in graphene/boron nitride/graphene heterostructures

A. Mishchenko, J. S. Tu, Y. Cao, R. V. Gorbachev, J. R. Wallbank, M.T. Greenaway, V. E. Morozov, S. V. Morozov, M. J. Zhu, S. L. Wong, F. Withers, C. R. Woods, Y.-J. Kim, K. Watanabe, T. Taniguchi, E. E. Vdovin, O. Makarovsky, T. M. Fromhold, V. I. Fal'ko, A. K. Geim, L. Eaves, K. S. Novoselov

1 Resonant tunnelling processes in graphene heterostructures

Here we describe the theoretical model for the tunnelling of Dirac electrons between two slightly misaligned graphene layers, separated by a thin layer of misaligned hBN [1–5]. Angles θ and θ_{BN}, $\theta \ll \theta_{BN}$, describe the misalignment of the top graphene layer, and the hBN layer, with respect to the bottom graphene layer. For the sake of simplicity, below we assume $|\theta| \ll |\theta_{BN}| \ll 1\,\mathrm{rad}$, and hence use $\boldsymbol{k}\cdot\boldsymbol{p}$ theory (here $\hbar = 1$). Also, we take into account that for $\theta_{BN} \gtrsim 0.04$ radians the energy scale $v_F|\sqrt{(\theta_{BN}^2+\delta^2)}\boldsymbol{K}|$ is beyond the Fermi energy obtainable by electrostatic doping (where $\delta \sim 1.8\%$ is the graphene-hBN lattice mismatch). Then, we model a heterostructure with graphene sheets separated by a single hBN layer, so that the $\boldsymbol{k}\cdot\boldsymbol{p}$ Hamiltonian is

$$H = \begin{pmatrix} H_T & H_{\mathrm{int},T} & 0 \\ H_{\mathrm{int},T}^{\dagger} & H_{BN} & H_{\mathrm{int},B}^{\dagger} \\ 0 & H_{\mathrm{int},B} & H_B \end{pmatrix}; \quad H_{l=T/B} = v_F \begin{pmatrix} U_l/v_F & \zeta k_x - ik_y \\ \zeta k_x + ik_y & U_l/v_F \end{pmatrix}; \quad H_{BN} = \begin{pmatrix} \epsilon_N & 0 \\ 0 & \epsilon_B \end{pmatrix}.$$

Here we use a basis of the Bloch functions $(\Phi_A^T,\Phi_B^T,\Phi_N^{BN},\Phi_B^{BN},\Phi_A^B,\Phi_B^B)$ taken at the $K(K')$-point, $\zeta = +(-)$, from the corresponding layer. The 2×2 blocks $H_{T/B}$ describe the Dirac electrons in the top (T) or bottom (B) graphene layers, with the voltage bias $U_T - U_B = \Delta\varphi$ included. H_{BN} describes states on the nitrogen (with energy ϵ_N) and boron (with energy ϵ_B) sublattices of the hBN layer. The coupling between the graphene layers ($l = T$ or B) and the hBN layer is adapted from Ref. [6] and similar theories of twisted two-layer graphene [7–12],

$$H_{int,l} = \frac{1}{3}\sum_{j=1,2,3} e^{-i\Delta\boldsymbol{K}_{T/B,j}^{\zeta}\cdot\boldsymbol{r}} \begin{pmatrix} \gamma_N & \gamma_B e^{-i\frac{2\pi}{3}(\zeta j-1)} \\ \gamma_N e^{i\frac{2\pi}{3}(\zeta j-1)} & \gamma_B \end{pmatrix}.$$

The momentum shift $\Delta\boldsymbol{K}^{\zeta}_{l,j} = \boldsymbol{K}^{\zeta}_{l,j} - \boldsymbol{K}^{\zeta}_{BN,j}$ describes the misalignment of the Brillouin zone corner of the hBN lattice, $\boldsymbol{K}^{\zeta}_{BN,j}$, from the Brillouin zone corners, $\boldsymbol{K}^{\zeta}_{l,j}$, of each of the graphene layers. The Brillouin zone corner label, j, is consistent with Fig. 1 of the main text. Also $\gamma_{N/B}$ are the hopping integral to the nitrogen sites (γ_N) or the boron sites (γ_B).

Next, we integrate out the hBN layer to obtain the effective Hamiltonian acting in the space of states in the two graphene layers,

$$H^{\text{eff}}(\epsilon) = \begin{pmatrix} H_T & 0 \\ 0 & H_B \end{pmatrix} + \delta H(\epsilon); \quad \delta H(\epsilon) \equiv \begin{pmatrix} \delta H_{TT} & \delta H_{TB} \\ \delta H^{\dagger}_{TB} & \delta H_{BB} \end{pmatrix} = \begin{pmatrix} H_{\text{int},T} \\ H_{\text{int},B} \end{pmatrix} \frac{1}{\epsilon - H_{BN}} \begin{pmatrix} H^{\dagger}_{\text{int},T} & H^{\dagger}_{\text{int},B} \end{pmatrix}.$$

The effect of the intralayer terms, δH_{TT} and δH_{BB}, consists in the formation of moiré minibands [13, 14], which modify graphene's spectra at energies $E \gtrsim v_F|\sqrt{(\theta^2_{BN} + \delta^2)}\boldsymbol{K}|$. For $\theta_{BN} \gtrsim 2^{\circ}$, this energy is higher than the energy where features in the current-voltage characteristics are formed for obtainable carrier densities in graphene, so that we only consider the effective interlayer hopping. For the same reason, we do not retain terms in $\delta H(\epsilon)$ that cause the wavevector transfer of finite hBN reciprocal lattice vector: this would scatter electrons to a high energy region of graphene's Brillouin zone that will not contribute to the tunnelling. Also, since we consider $|\epsilon| \ll |\epsilon_N|, |\epsilon_B|$, we find that

$$\delta H_{TB} = \frac{\gamma^{\text{eff}}}{3} \sum_{j=1,2,3} e^{-i\Delta\boldsymbol{K}^{\zeta}_j \cdot \boldsymbol{r}} \begin{pmatrix} 1 & e^{-i\frac{2\pi}{3}(\zeta j - 1)} \\ e^{i\frac{2\pi}{3}(\zeta j - 1)} & 1 \end{pmatrix}, \quad \text{where} \quad \gamma^{\text{eff}} = -\frac{\gamma_N^2}{3\epsilon_N} - \frac{\gamma_B^2}{3\epsilon_B}.$$

A magnetic field, $\boldsymbol{B}_{\parallel}$, applied in the plane of the device, results in an additional momentum transferred to the tunnelling electron, so that the momentum shift ($\Delta\boldsymbol{K}^{\zeta}_j = \boldsymbol{K}^{\zeta}_{T,j} - \boldsymbol{K}^{\zeta}_{B,j} \approx \theta\hat{\boldsymbol{l}}_z \times \boldsymbol{K}^{\zeta}_j$ for $\boldsymbol{B}_{\parallel} = 0$) becomes,

$$\Delta\boldsymbol{K}^{\zeta}_j = \boldsymbol{l}_z \times \left[\theta\boldsymbol{K}^{\zeta}_j + ed\boldsymbol{B}_{\parallel}\right], \tag{S.1}$$

with e the electron charge, $\boldsymbol{l}_z = (0, 0, 1)$, and d the separation between the two graphene layers. For a single-layer hBN tunnel junction we estimate $\gamma^{\text{eff}} \sim 10\,\text{meV}$ using assumptions from Ref. [6]. For a device with several hBN layers between the graphene sheets, we treat γ^{eff} as a phenomenological parameter which determines the size of the matrix elements between Dirac plane waves $|\psi^{T/B}_{\zeta,s_{T/B}}(\boldsymbol{k}_{T/B})\rangle = \frac{1}{\sqrt{2}}\left(1, \zeta s_{T/B} e^{i\zeta\phi_{\boldsymbol{k}_{T/B}}}\right) e^{i\boldsymbol{k}_{T/B}\cdot\boldsymbol{r}}$ in the two graphene layers (here $\phi_{\boldsymbol{k}} = \tan^{-1}(k_y/k_x)$ and $s_{T/B} = \pm 1$ is the band index),

$$\langle\psi^{T}_{\zeta,s_T}(\boldsymbol{k}_T)|\delta H_{TB}|\psi^{B}_{\zeta,s_B}(\boldsymbol{k}_B)\rangle = \frac{(2\pi)^2\gamma^{\text{eff}}}{3} \sum_{j=1,2,3} g\,\delta(\boldsymbol{k}_T - \boldsymbol{k}_B + \Delta\boldsymbol{K}^{\zeta}_j), \tag{S.2}$$

$$g = \frac{1}{2}\left(1 + \zeta s_B e^{-i\left(\frac{2\pi}{3}(\zeta j - 1) - \zeta\phi_{\boldsymbol{k}_B}\right)}\right)\left(1 + \zeta s_T e^{i\left(\frac{2\pi}{3}(\zeta j - 1) - \zeta\phi_{\boldsymbol{k}_T}\right)}\right).$$

Then, the Fermi golden rule for the current density, formed by the tunnelling of electron plane

waves between the two graphene flakes reads,

$$J = \frac{-eg_s}{(2\pi)^3} \sum_{\zeta, s_B, s_T} \int d\boldsymbol{k}_B d\boldsymbol{k}_T \frac{1}{\pi} \mathrm{Im} \frac{|\langle \psi^T_{\zeta,s_T}(\boldsymbol{k}_T)|\delta H_{TB}|\psi^B_{\zeta,s_B}(\boldsymbol{k}_B)\rangle|^2}{s_T v_F|\boldsymbol{k}_T| + \Delta\varphi - s_B v_F|\boldsymbol{k}_B| - i\gamma} (f^{\mu_B}_{s_B,\boldsymbol{k}_B} - f^{\mu_T}_{s_T,\boldsymbol{k}_T}). \tag{S.3}$$

Here $g_s = 2$ accounts for spin degeneracy, and $f^{\mu_{T/B}}_{s_{T/B},\boldsymbol{k}_{T/B}}$ are the occupancy numbers written using the chemical potentials $\mu_{T/B}$ on the two layers. Also, we take into account a finite broadening, γ, of electron states.

In the limit $\gamma \to 0$ the allowed tunnelling processes for electrons in each valley must simultaneously conserve both energy and momentum:

$$s_T v_F|\boldsymbol{k}_B - \Delta\boldsymbol{K}^\zeta_j| + \Delta\varphi - s_B v_F|\boldsymbol{k}_B| = 0.$$

This constraint is clearly seen in Supplementary Fig. 1, which shows the dependence of the current density on the band offset $\Delta\varphi$ for $\theta = 0.5°$ (correspondingly $v_F|\Delta\boldsymbol{K}^\zeta_j| = 0.1\,\mathrm{eV}$). The right panel of each insets shows the relative alignment of the Dirac cones on the bottom layer (grey) and the top layer (blue), for particular values of $\Delta\varphi$. The left panels show the contribution to the current density arising from states in the valley K for electrons on the bottom layer. Here the four sub-panels correspond to tunnelling between the bands: conduction to conduction, valence to conduction, valence to valence, and conduction to valence (listed clockwise from top left). The contribution of states with momentum near the valley K' can be described by rotating these images through 60°. In the absence of a magnetic field, graphene's two valleys make the same contribution to the current density, whereas in a finite $\boldsymbol{B}_\parallel$ this valley degeneracy is lifted. Depending on the value of $|\Delta\varphi| - v_F|\Delta\boldsymbol{K}^\zeta_j|$ we find that:

(i) For $|\Delta\varphi| \geq v_F|\Delta\boldsymbol{K}^\zeta_j|$ the wavevectors lie on an ellipse parametrised by $0 \leq \phi \leq 2\pi$,

$$\boldsymbol{k}_B = \begin{pmatrix} \sqrt{\frac{(\Delta\varphi/v_F)^2 - |\Delta\boldsymbol{K}^\zeta_j|^2}{4}} \sin(\phi) \\ \frac{|\Delta\varphi|}{2v_F}\cos(\phi) + \frac{|\Delta\boldsymbol{K}^\zeta_j|}{2} \end{pmatrix}, \qquad \begin{matrix} s_B = 1,\ s_T = -1 \text{ for } \Delta\varphi > 0 \\ s_B = -1,\ s_T = 1 \text{ for } \Delta\varphi < 0. \end{matrix} \tag{S.4}$$

This is exemplified in Supplementary Fig. 1 (a,b) which show that the dominant contribution to the current density arises from the three ellipses described by $2\pi/3$ rotations of Eq. (S.4), where the chirality factor g in Eq. S.2 modulates the tunnelling efficiency along the perimeter of each ellipse.

(ii) For $|\Delta\varphi| \leq v_F|\Delta\boldsymbol{K}^\zeta_j|$ the states lie on a hyperbola parametrised by $-\infty \leq \chi \leq \infty$,

$$\boldsymbol{k}_B = \begin{pmatrix} \sqrt{\frac{|\Delta\boldsymbol{K}^\zeta_j|^2 - (\Delta\varphi/v_F)^2}{4}} \sinh(\chi) \\ s_B \frac{\Delta\varphi}{2v_F}\cosh(\chi) + \frac{|\Delta\boldsymbol{K}^\zeta_j|}{2} \end{pmatrix}, \qquad \text{for } s_B = s_T = 1 \text{ and } s_B = s_T = -1 \tag{S.5}$$

This is exemplified in Supplementary Fig. 1 (e-f) where only half of each hyperbola is visible due to the chirality of the electron states in graphene.

(iii) Insets (c,d) in Supplementary Fig. 1, single out the special case $|\Delta\varphi| = v_F|\Delta\boldsymbol{K}^\zeta_j|$. Here

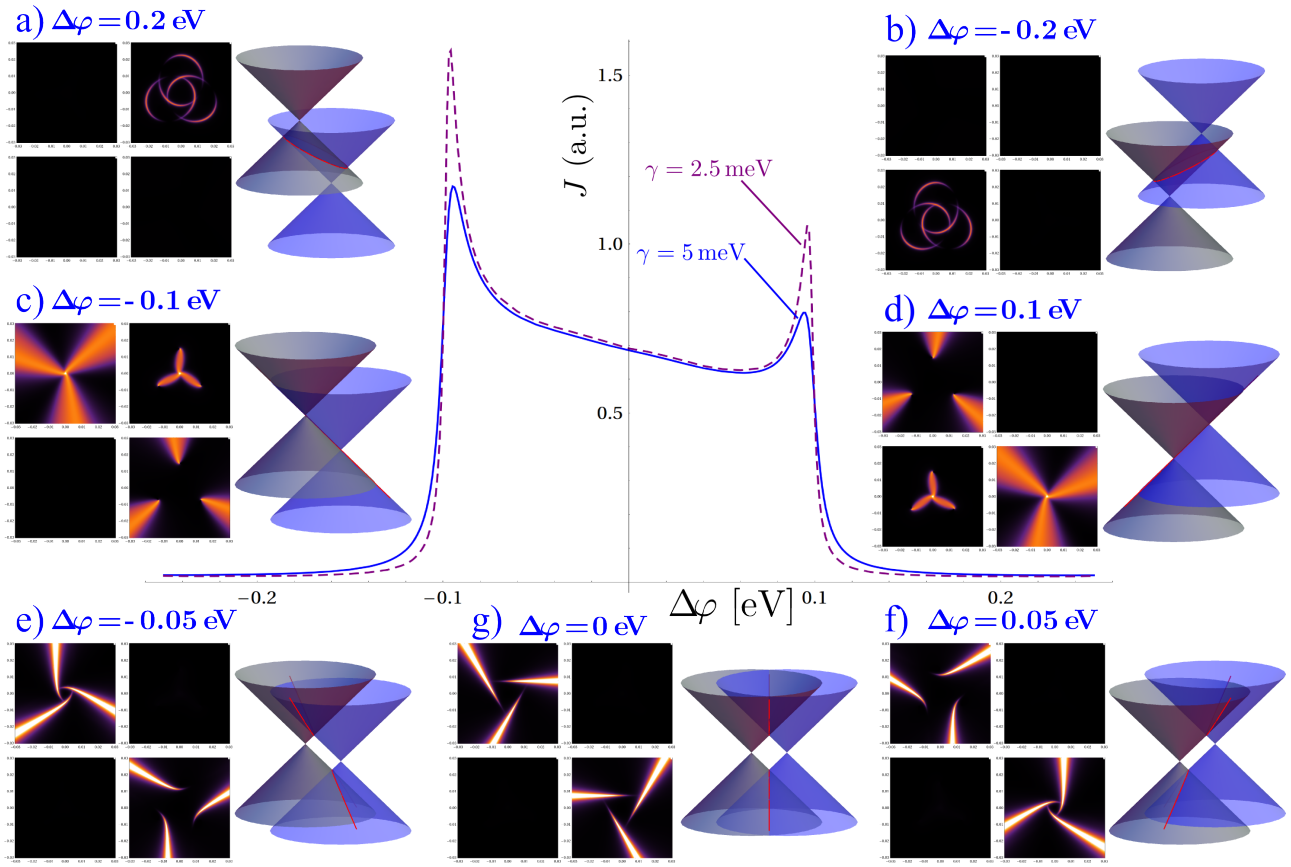

Supplementary Fig. 1: Dependence of the current density on band offset $\Delta\varphi$ for $\theta = 0.5°$, $B_{\|} = 0$, and $\mu_B = -\mu_T = 0.5\,\mathrm{eV}$. The insets, calculated for $\gamma = 5\,\mathrm{meV}$, show the contribution to the current density arising from states with momentum $\boldsymbol{k}_B$ in valley K of the bottom layer (see discussion in text).

the wavevectors lie on the straight lines separating elliptical (i) and hyperbolic regimes (ii). These give rise to sharp peaks in the current, the height and width of which is controlled by the broadening γ.

2 Electrostatics and the current-voltage characteristics of graphene based tunnelling transistors

The electrostatic properties of the device can be described in terms of a three-plate capacitor model. The doped n-Si (plate) is separated from the bottom graphene layer by a 290 nm-thick silicon oxide barrier and a 30 nm-thick hBN substrate layer. A hBN tunnel barrier, a few atomic layers thick, separates the two graphene electrodes. The electric field generated by charge on the gate electrode is only partly screened by the lower graphene layer, due to graphene's low density of electronic states when the chemical potential is close to the neutrality (Dirac) point. For the case of chemically undoped graphene layers which, to a good approximation, is the case in our devices, it can be shown that the bias voltage, V_b, the gate voltage, V_g, and the chemical potentials in the top (μ_T) and bottom (μ_B) graphene layers are related by the following

equation:

$$\frac{e^2 d n_T}{\epsilon_{BN}\epsilon_0} + \mu(n_T) + \mu(n_T - n_{ext}(V_g)) + eV_b = 0, \tag{S.6}$$

or equivalently, $\Delta\varphi + \mu_T - \mu_B + eV_b = 0$. Here ϵ_0 is the vacuum permittivity, d and ϵ_{BN} are the thickness and dielectric constant of hBN, respectively, and $\mu_T = \mu(n_T)$ and n_T are the Fermi energy and sheet carrier density in the top graphene electrode. The chemical potential has a square-root dependence on carrier density, n, given by $\mu(n) = \pm v_F\sqrt{\pi|n|}$. The gate-induced carrier density on the doped n-Si layer, $n_{ext}(V_g)$ is defined by the gate capacitance and gate voltage. The term $\Delta\varphi/e$ is the electrostatic voltage drop between the two graphene layers and represents the classical capacitance of the device. The Dirac cones are displaced in energy by an amount $\Delta\varphi$. The second and third terms in Eq. S.6 result from the quantum capacitance of the top and bottom graphene layers respectively [15]. By changing the bias and gate voltages, the electrochemical potentials ($\mu_{T,B}$) of the graphene layers can be adjusted interdependently.

In Supplementary Fig. 2 we have employed the electrostatic model, Eq. (S.6), to recalculate the parameters μ_B, μ_T and $\Delta\varphi$, used in Eq. (S.3), into the gate and bias voltages V_g and V_b. Supplementary Fig. 2 (a) displays the zero-magnetic-field current density J/J_0 and the differential currents $\frac{dI}{dV_b}R_0$ and $\frac{dI^2}{dV_b^2}R_1^2$, normalised to their peak values J_0, R_0^{-1}, and $R_1^{-1/2}$ obtained at the values of V_b and V_g marked by a white crosses in the figure. Maxima in J/J_0 and corresponding features in $\frac{dI}{dV_b}R_0$ and $\frac{dI^2}{dV_b^2}R_1^2$, occur along such lines on the V_b-V_g plane that $|\Delta\varphi| = v_F|\Delta\boldsymbol{K}_j^\zeta|$, and are visible in the main panels of Supplementary Fig. 2(a). Features corresponding to the characteristic lines $\mu_{T/B} = 0$ and $\mu_{T/B} = (\Delta\varphi \pm v_F|\Delta\boldsymbol{K}_j^\zeta|)/2$ (discussed in main text) are more clearly visible in the insets in Supplementary Fig. 2.

Supplementary figures 2 (b,c) show the normalised current density for two orientations of the in-plane magnetic field, $B_\parallel = 15\,\mathrm{T}$. Here the length of the in-plane wavevector transferred upon tunnelling ($|\Delta\boldsymbol{K}_j^\zeta|$, Eq. (S.1)) may be different for each of the six Brillouin zone corners $\boldsymbol{K}_j^\zeta$. Hence the features associated with the characteristic lines $|\Delta\varphi| = v_F|\Delta\boldsymbol{K}_j^\zeta|$ and $\mu_l = (\Delta\varphi \pm v_F|\Delta\boldsymbol{K}_j^\zeta|)/2$ (which depend on $|\Delta\boldsymbol{K}_j^\zeta|$) are split into multiple features in Supplementary Fig. 2(b,c). Note that the higher value of broadening, $\gamma = 40\,\mathrm{meV}$, in Supplementary Fig. 3 (d,f) of the main text, as compared to $\gamma = 5\,\mathrm{meV}$ in Supplementary Fig. 2, obscures the above mentioned peak splitting so that the effect of the magnetic field is more subtle. This is illustrated in Supplementary Fig. 3, which displays the normalised current, for cuts in the V_g-V_b plane at constant gate voltage, for both $\gamma = 5\,\mathrm{meV}$ (panels a-c) and $\gamma = 40\,\mathrm{meV}$ (panels d-f).

3 Crystallographic alignment of graphene layers

Devices were fabricated using the standard dry-transfer procedure [16], with one critical step added: during transfer the crystallographic orientations of the two graphene flakes were aligned to within 2°, see 4e. To this end, for the device fabrication we selected mechanically exfoli-

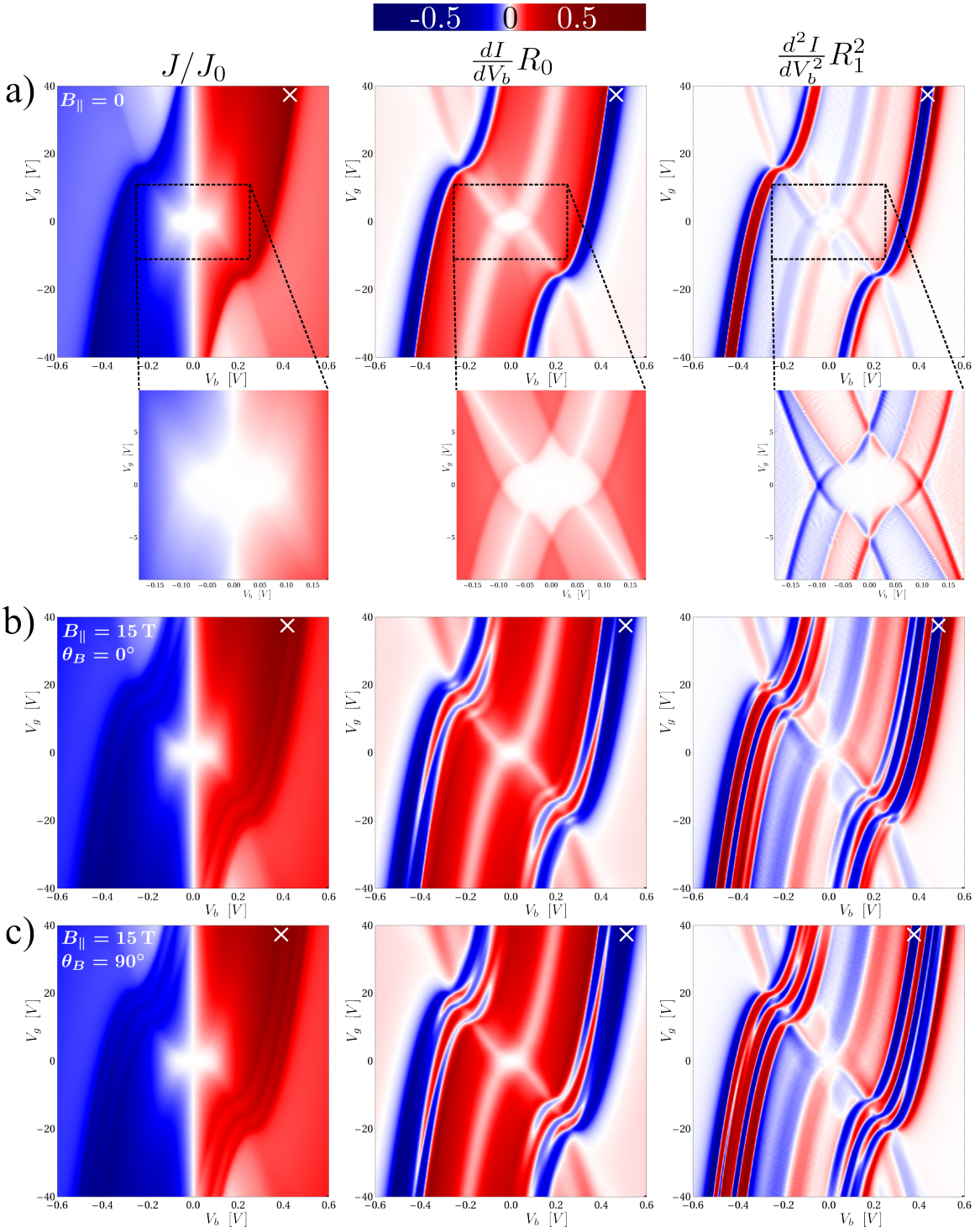

Supplementary Fig. 2: a) The current density J/J_0 and the differential currents $\frac{dI}{dV_b}R_0$ and $\frac{dI^2}{dV_b^2}R_1^2$, normalised to their peak values J_0, R_0^{-1}, and $R_1^{-1/2}$ obtained at the values of V_b and V_g marked by a white crosses. Insets show the enlargement of the regions marked with dashed lines. b-c) The same as (a) but including 15 T in-plane magnetic fields oriented either perpendicular ($\theta_B = 0°$) or parallel ($\theta_B = 90°$) to the carbon-carbon bonds in the bottom graphene layer (zig-zag or armchair directions).

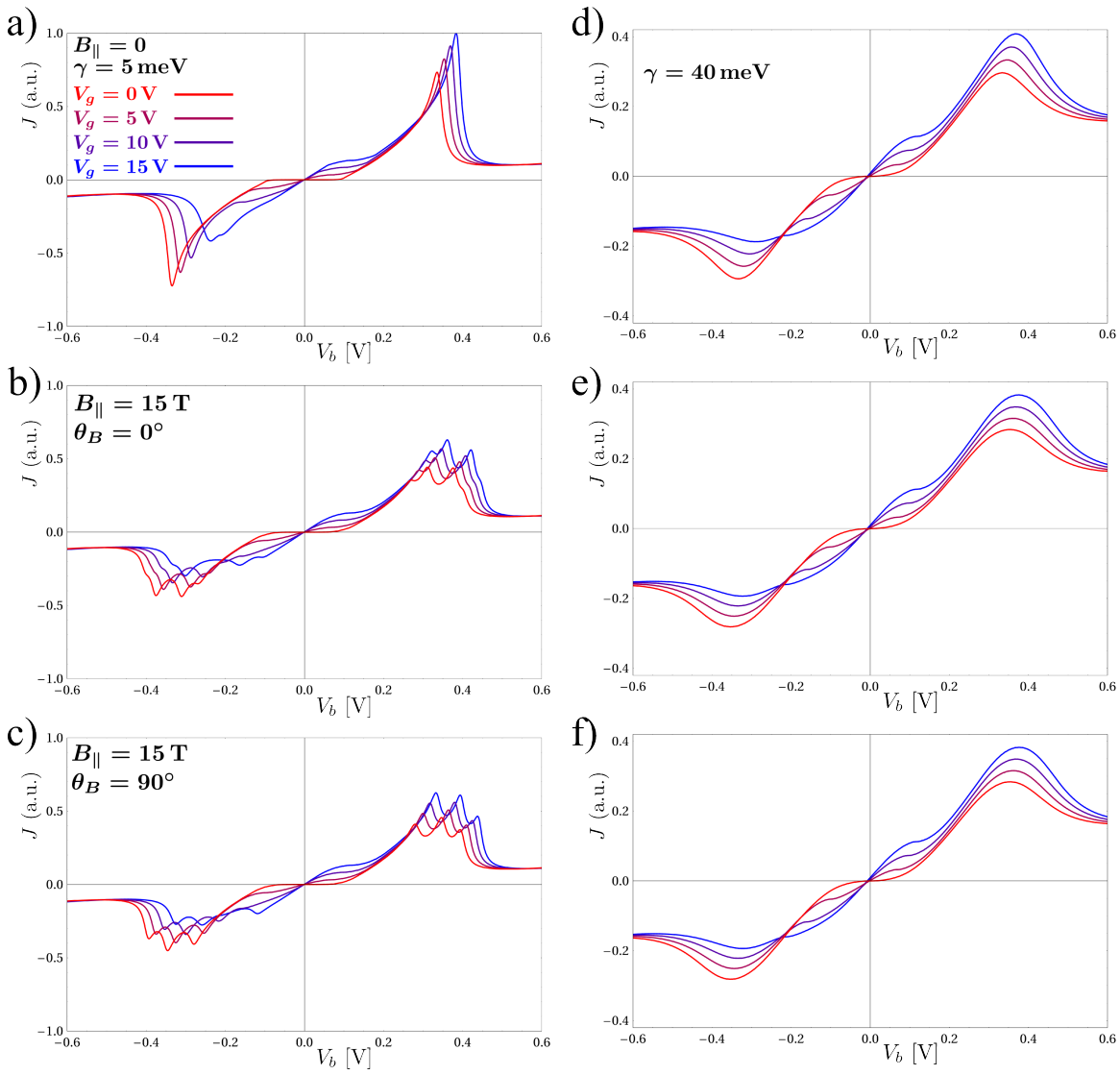

Supplementary Fig. 3: The dependence of the current density (normalised to its highest obtained value in (a)) for various gate voltages. Results are shown for the broadening $\gamma = 5\,\mathrm{meV}$ and $B_\parallel = 0$ as well as for two orientations of a 15 T in-plane magnetic field (b,c). Panels (d-f) show the same as (a-c) but for $\gamma = 40\,\mathrm{meV}$.

ated graphene flakes with edges oriented along crystallographic directions (so the facets of the flakes comprise angles of multiples of 30°). Typically we use narrow ribbons (few micrometre across) as the top and bottom graphene electrodes, so they form a junction of several square micrometres in area at the place of their crossing, when oriented at 90° to each other.

We employ Raman spectroscopy in order to distinguish between zig-zag and armchair edges and thus determine the crystallographic orientation of flakes with well-defined facets. It has been shown previously [17] that the zig-zag edge of graphene should not produce any D peak, in contrast to armchair edge. In reality, because the graphene edges are not perfect (even though predominantly oriented) the typical ratio for the amplitude of the D peak from armchair and zig-zag edges is around 1.5, Supplementary Fig. 4c,d [18].

Raman spectroscopy was performed at room temperature in the backscattering geometry using a Renishaw inVia Raman microscope. A grating with 2400 lines mm^{-1} was used, providing a spectral resolution of ± 1 cm^{-1}. An excitation laser source of 514 nm with power less than 0.7 mW was used in the measurements, using a 100x objective. The excitation source is linearly polarised in the horizontal direction of the sample plane. No peak evolution due to heating or beam damage were observed during each individual scan. Peak intensity maps were obtained from fits of the graphene-associated Raman D peak with baseline corrections accounted for.

Supplementary Fig. 4a,b presents the spatial map of the Raman D peak amplitude for the top and bottom flakes. By comparing the amplitude of the D peak from the long edges of the top and bottom graphene electrodes (4d) we confirm that they most probably have different chirality (zig-zag for the top graphene electrode and armchair for the bottom), which confirms that the two electrodes are crystallographically aligned.

Moreover, it has been demonstrated previously that due to the reconstruction of graphene lattice, the Raman spectrum of graphene on hBN changes [19] if the misorientation angle between the two crystals is less than 5°. In particular, the 2D peak becomes significantly broadened. This gives one a tool to determine the relative orientation of graphene with respect to hBN.

By comparing the broadening of the 2D peak of the top and bottom graphene electrodes (in case they both rest on the same monocrystalline flake of hBN) one can conclude on the relative orientation between the two electrodes. This technique, however, is limited to the cases when crystallographic orientation of the graphene flakes is within 5° with respect to that of hBN.

Supplementary Fig. 5 presents measurements of the broadening of the 2D peak for the top and bottom graphene for the device presented in Supplementary Fig. 4. Measurements suggest that the top and bottom graphene crystals are aligned to the crystallographic orientation of the underlying substrate hBN by $\pm 2°$ and $\pm 3°$ degrees respectively. This means that the graphene layers are misoriented with respect to each other either by 1 degree (if the sign of misorientation to hBN is the same) or by 5 degrees (if the misorination to hBN is of the opposite signs). The position of the resonances in the tunnelling current suggest that indeed, the flakes are misoriented by 1°.

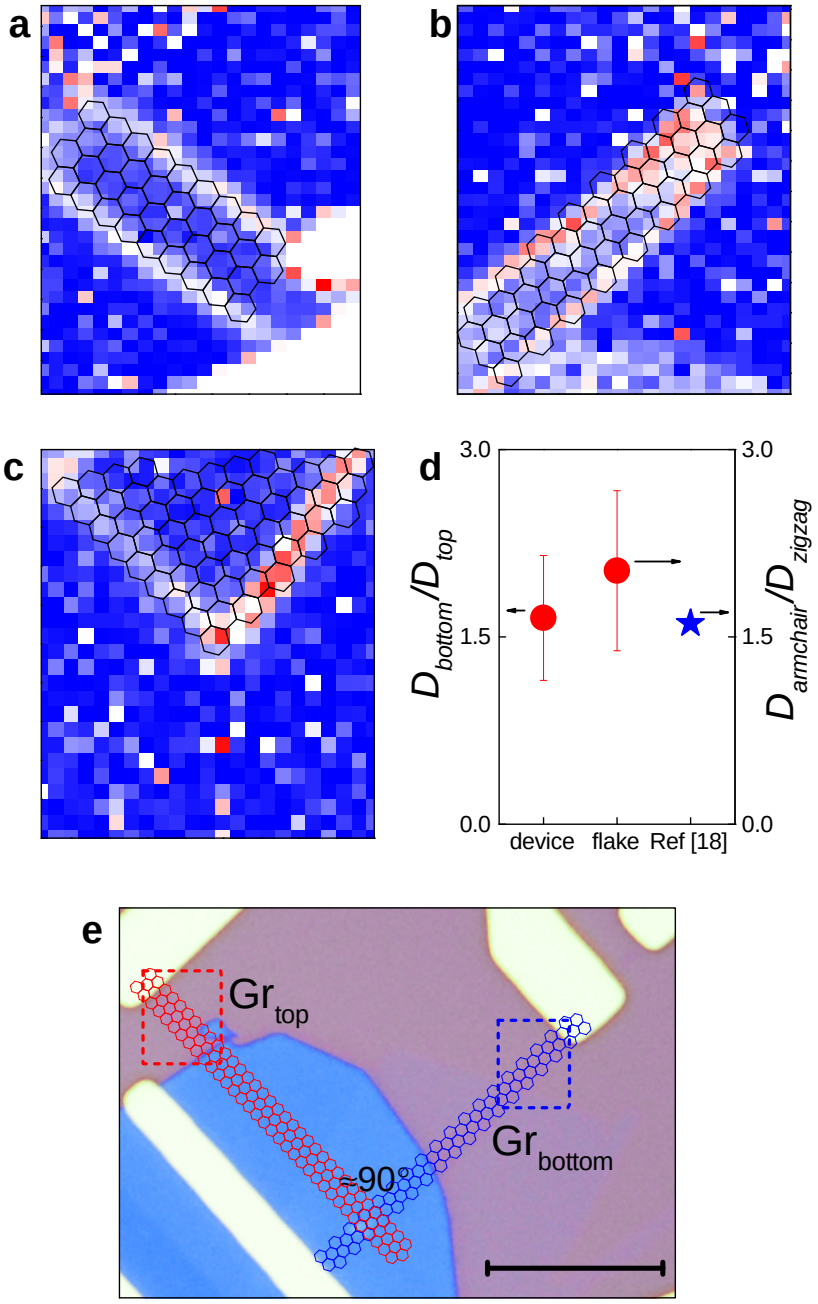

Supplementary Fig. 4: Crystallographic alignment of the two graphene layers in the resonant tunnelling device (shown in panel (e)). Panels (a-c) show Raman D peak intensity maps - top (a) and bottom (b) graphene layers for device, and mechanically exfoliated graphene flake (c) with 90° angle between edges. Laser is linearly polarized along horizontal axis. Panel (d) is the D peak intensity ratio between armchar to zigzag edges. Panel (e) is the optical micrograph of the studied device, scale bar 10 μm. Red and blue rectangles outline regions mapped on panels (a) and (b), respectively.

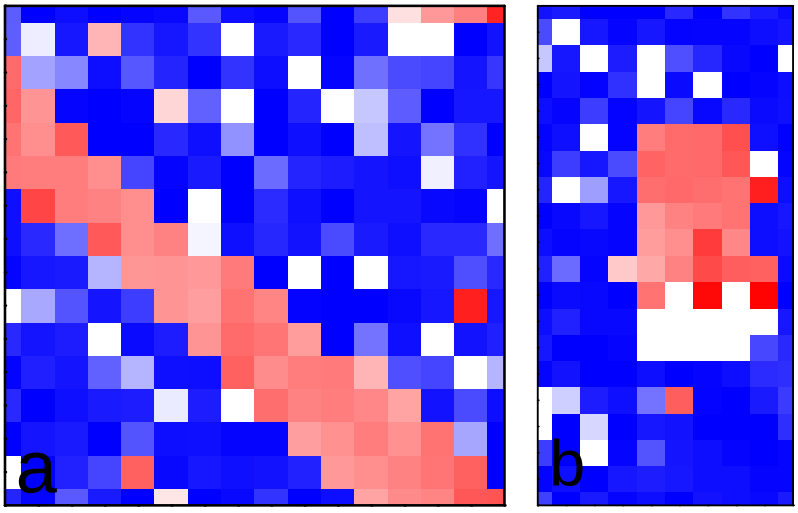

Supplementary Fig. 5: Crystallographic alignment of the two graphene layers in the resonant tunnelling device (device shown in 4e). Panels show Raman 2D peak full width at half maximum maps: top (a) and bottom (b) graphene layers for device. Scale: blue to white to red, 0 to 15 to 30 cm^{-1}. Pixel size is 0.5 μm.

4 Results obtained for other devices

We fabricated several aligned devices. The data for one of the devices is presented in the main text. Supplementary Fig. 6 shows $J - V_b$ characteristics as well as contour plots of dI/dV_b and d^2I/dV_b^2 for two more aligned devices.

5 Room Temperature Operation

In Supplementary Fig. 7 we demonstrate the room temperature operation of the device presented in the main text.

6 Comparison with resonant tunnelling in conventional resonant tunnelling devices

Previously, it has been demonstrated that graphene/hBN/graphene devices should not exhibit instabilities which would result in intrinsic oscillations [20]. In conventional double barrier resonant tunnelling devices (DBRTDs), the build-up of charge in the quantum well leads to a delay of the current with respect to the voltage which can be represented in terms of an inductance in the equivalent circuit of the device [21–23]. This effective inductance, which is an important feature in the operation of DBRTD oscillators, is absent in our single barrier devices [20].

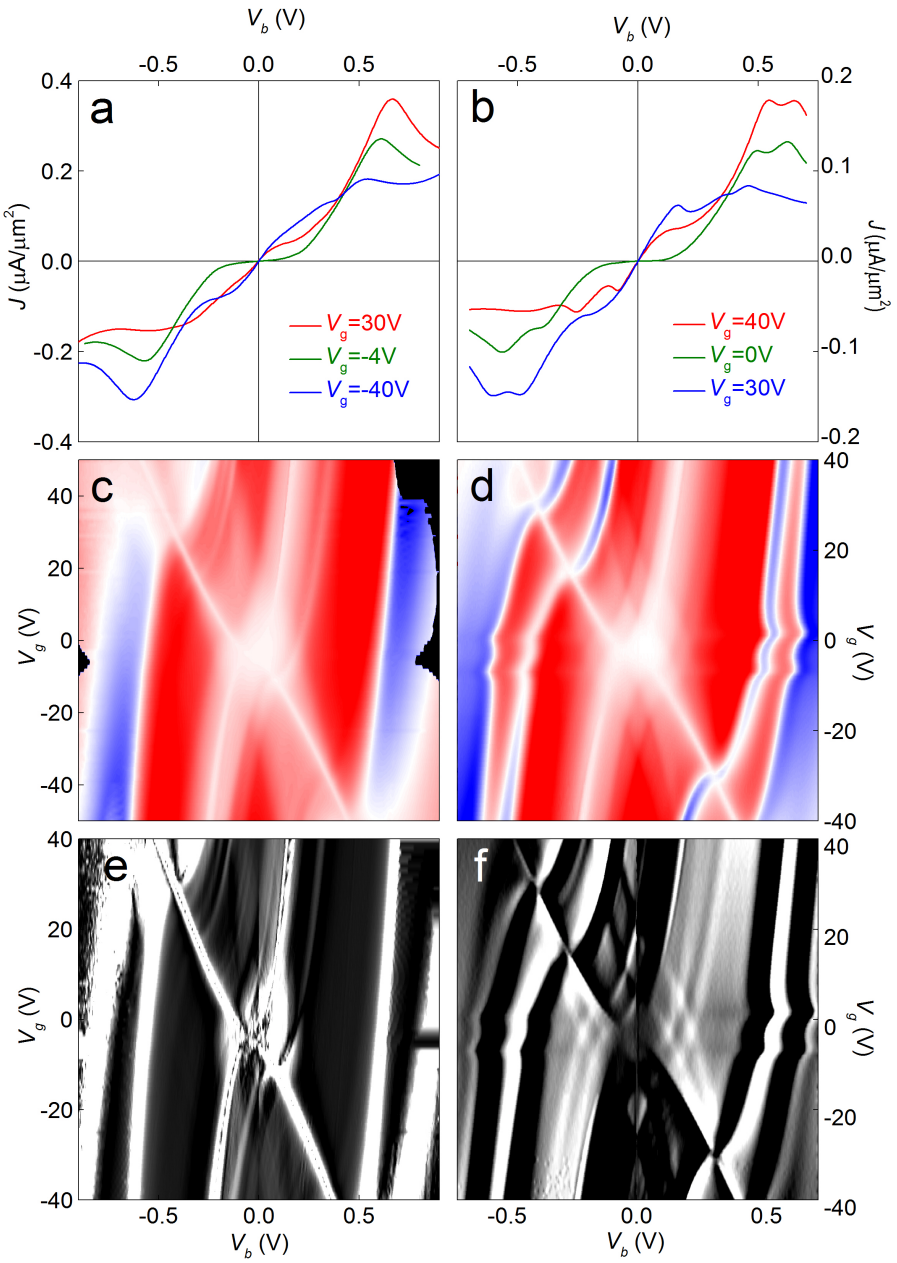

Supplementary Fig. 6: Tunnelling characteristics of two additional devices with different misalignment angles. $T = 2\,\mathrm{K}$. Left panels - device with 0.9° misalignment angle, right panels - device with two misalignment angles: 0.6° and 1.1°, possibly due to the presence of a large bubble in the active area of device. a) and b) $J - V_b$ characteristics, c) and d) dI/dV_b contour plots, e) and f) $|d^2I/dV_b^2|$ contour plots. Device area: $120\,\mu\mathrm{m}^2$ for a, c, e and $100\,\mu\mathrm{m}^2$ for b, d, f.

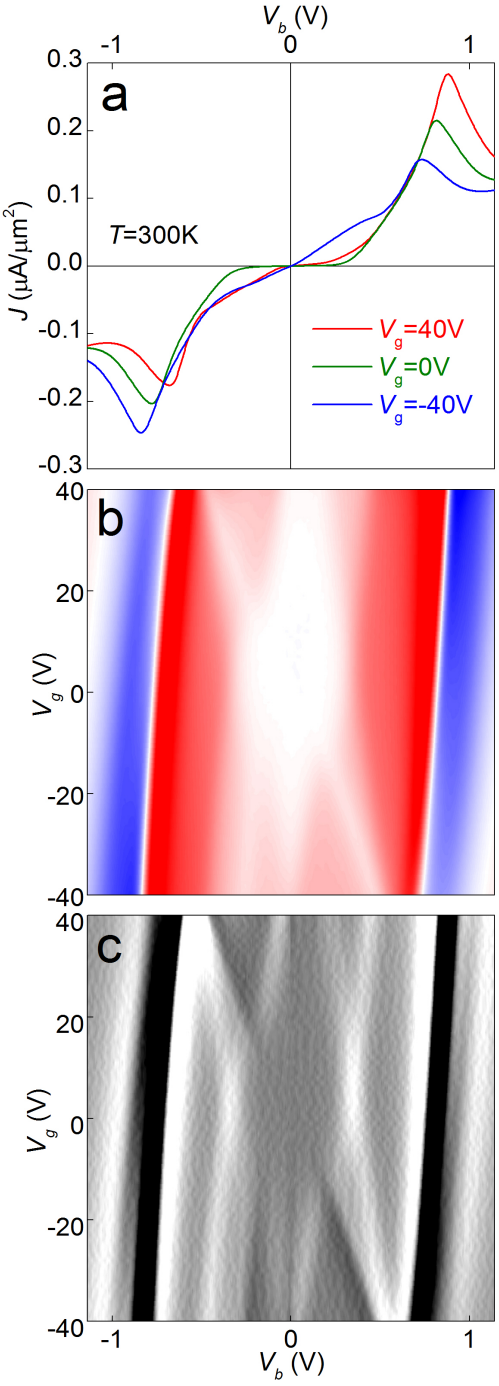

Supplementary Fig. 7: Tunnelling characteristics of the device presented in main text, measured at 300 K. a) $J - V_b$ characteristics, b) dI/dV_b contour plot, c) $|d^2I/dV_b^2|$ contour plot.

References

[1] Feenstra, R. M., Jena, D. and Gu, G. Single-particle tunneling in doped graphene-insulator-graphene junctions. *J. Appl. Phys.* **111**, 043711 (2012).

[2] Vasko, F. T. Resonant and nondissipative tunneling in independently contacted graphene structures. *Phys. Rev. B* **87**, 075424 (2013).

[3] Barrera, S. C., Gao, Q. and Feenstra, R. M. Theory of graphene-insulator-graphene tunnel junctions. *J. Vac. Sci. Technol. B* **32**, 04E101 (2014).

[4] Wallbank, J. R. *Electronic Properties of Graphene Heterostructures with Hexagonal Crystals* (Springer PhD Thesis Series, Springer, 2014); ISBN 978-3-319-07721-5.

[5] Brey, L. Coherent tunneling and negative differential conductivity in graphene-hBN-graphene heterostructure. *Phys. Rev. Applied* **2**, 014003 (2014).

[6] Kindermann, M., Uchoa, B. and Miller, D. L. Zero-energy modes and gate-tunable gap in graphene on hexagonal boron nitride. *Phys. Rev. B* **86**, 115415 (2012).

[7] Lopes dos Santos, J. M. B., Peres, N. M. R., and Castro Neto, A. H. Graphene Bilayer with a Twist: Electronic Structure. *Phys. Rev. Lett.* **99**, 256802 (2007).

[8] Bistritzer, R. and MacDonald, A. H. Transport between twisted graphene layers. *Phys. Rev. B* **81**, 245412 (2010).

[9] Kindermann, M. and First, P. N. Local sublattice-symmetry breaking in rotationally faulted multilayer graphene. *Phys. Rev. B* **83**, 045425 (2011).

[10] Bistritzer, R. and MacDonald, A. H. Moiré butterflies in twisted bilayer graphene. *Phys. Rev. B* **84**, 035440 (2011).

[11] Mele, E. J. Band symmetries and singularities in twisted multilayer graphene. *Phys. Rev. B* **84**, 235439 (2011).

[12] Lopes dos Santos, J. M. B., Peres, N. M. R. and Castro Neto, A. H. Continuum model of the twisted graphene bilayer. *Phys. Rev. B* **86**, 155449 (2012).

[13] Ortix, C., Yang, L. and van den Brink, J. Graphene on incommensurate substrates: Trigonal warping and emerging Dirac cone replicas with halved group velocity. *Phys. Rev. B* **86**, 081405 (2012).

[14] Wallbank, J. R., Patel, A. A., Mucha-Kruczynski, M., Geim, A. K., and Fal'ko, V.I. Generic miniband structure of graphene on a hexagonal substrate. *Phys. Rev. B* **87**, 245408 (2013).

[15] Yu, G. L., Jalil, R., Belle, B., Mayorov, A. S., Blake, P., Schedin, F., Morozov, S. V., Ponomarenko, L. A., Chiappini, F., Wiedmann, S., Zeitler, U., Katsnelson, M. I., Geim, A. K., Novoselova, K. S., Eliasa, D. C. Interaction phenomena in graphene seen through quantum capacitance. *Proc. Natl. Acad. Sci. U.S.A.* **110**, 3282, (2013).

[16] Ponomarenko, L. A., Geim, A. K., Zhukov, A. A., Jalil, R., Morozov, S. V., Novoselov, K. S., Grigorieva, I. V., Hill, E. H., Cheianov, V. V., Falko, V. I., Watanabe, K., Taniguchi, T., Gorbachev, R. V. Tunable metal-insulator transition in double-layer graphene heterostructures. *Nat. Phys.* **7**, 958 (2011).

[17] Casiraghi, C., Hartschuh, A., Qian, H., Piscanec, S., Georgi, C., Fasoli, A., Novoselov, K. S., Basko, D. M., Ferrari, A. C. Raman Spectroscopy of Graphene Edges. *Nano Letters* **9**, 1433 (2009).

[18] Neubeck, S., You, Y. M., Ni, H., Blake, P., Shen, Z. X., Geim, A. K., Novoselov, K. S. Direct determination of the crystallographic orientation of graphene edgesby atomic resolution imaging. *Apl. Phys. Lett.* **97**, 053110 (2010).

[19] Eckmann, A., Park, J. S., Yang, H. F., Elias, D., Mayorov, A. S., Yu, G. L., Jalil, R., Novoselov, K. S., Gorbachev, R. V., Lazzeri, M., Geim, A. K., Casiraghi, C. Raman Fingerprint of Aligned Graphene/h-BN Superlattices. *Nano Letters* **13**, 5242 (2013).

[20] Ryzhii, V., Satou, A., Otsuji, T., Ryzhii, M., Mitin, V., Shur, M. S. Dynamic effects in double graphene-layer structures with inter-layer resonant-tunnelling negative conductivity. *J. Phys. D: Appl. Phys.* **46**, 315107 (2013).

[21] Frensley, W. R. Quantum transport calculation of the smallsignal response of a resonant tunneling diode. *Apl. Phys. Lett.* **51**, 448 (1987).

[22] Mains, R. K., Haddad, G. I. Timedependent modeling of resonanttunneling diodes from direct solution of the Schrdinger equation. *J. Appl. Phys.* **64**, 3564 (1988).

[23] Mizuta, H., Tanoue, T. *The physics and applications of resonant tunnelling diodes*, 134-140 (Cambridge University Press, 1995).